



Using an Artificial Neural Network for Nondestructive Evaluation of the Heat Treating Processes for D2 Tool Steels

S. Kahrobaee, S. Ghanei, and M. Kashefi

(Submitted January 2, 2017; in revised form March 21, 2019)

In nondestructive evaluation (NDE) of heat-treated steels, different variables of the heat treating process have complex effects on outputs of NDE methods, and hence, the effect of one desired variable on NDE outputs should be evaluated to help interpreting the changes. In the present paper, the potential of the magnetic hysteresis method was evaluated for simultaneous detection of the austenitizing and tempering temperatures of AISI D2 samples parts subjected to different heat treatment conditions. To produce the microstructural changes, five groups of the samples were austenitized at 1025–1130 °C, quenched in oil and finally each group was tempered in the range 200–650 °C. SEM and x-ray diffractometry techniques were used to characterize different produced microstructures. For accurate and simultaneous prediction of tempering and austenitizing temperatures, an artificial neural network (ANN) was implemented for magnetic hysteresis outputs including magnetic saturation, coercivity and maximum differential permeability. The study revealed that the magnetic NDE system coupled to ANN has the ability to be adopted as an effective expert NDE tool to predict heat treatment effects on D2 tool steels.

Keywords AISI D2 steel, artificial neural network, austenitizing temperature, nondestructive testing, tempering temperature

1. Introduction

AISI D2 cold work tool steel is a high-carbon high-chromium tool steel alloyed with molybdenum and vanadium which is characterized by its superior mechanical and tribological properties such as high stability in hardening, high compressive strength, good through-hardening properties, good resistance to tempering back and high wear resistance. There are many industrial applications of D2 steel such as manufacturing of piercing and blanking dies, shear blades, wood milling cutters, as well as tools for punching, clipping, fine-blanking and spinning (Ref 1). Its desired properties are normally gained by obtaining a controlled microstructure through proper design of the heat treatment process.

Gaining proper mechanical properties needs performing a set of recommended heat treating steps including annealing (at 800 °C), stress relieving (at 650–700 °C), hardening (austenitizing at 1000–1080 °C and quenching in air or oil) and

tempering (200–550 °C) (Ref 2). The most important factors of the heat treating process are austenitizing and tempering temperatures which significantly affect the final mechanical properties. Increasing austenitizing temperature normally alters retained austenite percentage in the resultant microstructure due to more dissolving of alloying elements in austenitic matrix (Ref 3). In addition, five stages take place during tempering of these steels depending on the tempering temperature: ϵ carbides precipitates (Ref 4) and cementite forms (Ref 5) at lower tempering temperatures (200 to 300 °C) while decomposition of produced retained austenite (Ref 6) and secondary hardening phenomena (Ref 7) occur in higher tempering temperatures (400 to 500 °C), and at very high tempering temperatures (600 to 650 °C) spheroidized carbides (Ref 8) can be developed in the microstructure. Therefore, determination of desirable temperatures for austenitizing and tempering treatments as an accurate design for the process has a great influence on the final microstructure and mechanical properties.

Over the last decade, various electromagnetic NDE methods with different potentials have been introduced to characterize the material's features. For instance, magnetic Barkhausen noise (MBN) method for measuring residual stress/applied stress (Ref 9–11) and determining microstructural characteristics (Ref 12, 13), pulsed magnetic reluctance/pulsed magnetic flux leakage (PMFL/PMR) sensors for characterizing surface and subsurface defects (Ref 14) and hysteresis loop technique for assessing the microstructural variations in the bulk (Ref 15) are conventional methodologies used for nondestructive characterization of ferromagnetic materials. Besides, pulsed/conventional eddy current (PEC/EC) methods have been utilized to detect thickness (Ref 16) subsurface cracks (Ref 17) and microstructural changes (Ref 18, 19) at a certain depth below the surface of conductive materials.

S. Kahrobaee, Department of Mechanical and Materials Engineering, Sadjad University of Technology, P.O. box 91881-48848, Mashhad, Iran; **S. Ghanei**, Institute for Frontier Materials (IFM), Deakin University, Geelong, VIC 3216, Australia; and **M. Kashefi**, Department of Materials Engineering, Faculty of Engineering, Ferdowsi University of Mashhad, Mashhad, Iran. Contact e-mail: kahrobaee@sadjad.ac.ir and Saeed.kahrobaee@yahoo.com.

In magnetic nondestructive characterization of the heat-treated steels, microstructural changes are evaluated by applying one effective parameter. This is because different parameters have various effects on output of NDE methods, which makes establishing a relation between heat treating parameters and the outputs difficult. For example, surface carbon content in carburized steels subjected to different carbon potentials of the furnace but in a same carburizing process (for 8 h in 900 °C) was characterized by the EC method (Ref 20). Microstructural changes resulted from tempering treatment at different temperatures, for SAE 5140 and AISI D2 steels at constant austenitizing temperatures, have been assessed by MBN technology (Ref 21, 22). EC method has been utilized to assess development of tempered martensite embrittlement in hardened 4340 steels (which have been austenitized at a constant temperature of 1050 °C) after tempering in the range of 240-550 °C (Ref 23). The microstructural features of M250 maraging steel have also been studied during various thermal aging times (3-10 h) at a constant temperature of 482 °C using MBN and EC methods (Ref 24, 25). Determination of martensite percentage in dual-phase (DP) steel parts subjected to different intercritical annealing temperatures at a fixed time and chemical composition has been assessed by EC method (Ref 26). Ferrite grain size in DP steels due to different primary austenitizing processes with a constant martensite fraction has been determined using EC and MBN technologies (Ref 27), and the microstructural changes during employing different tempering temperatures for these kinds of steels intercritically annealed at a fixed temperature (832 °C) have been characterized by MBN method (Ref 28).

In the present paper, applying wide ranges of austenitizing (1000-1130 °C) and tempering (200-650 °C) temperatures, the application of magnetic hysteresis method for simultaneous detection of the austenitizing and tempering temperatures of AISI D2 parts with unknown heat treatment conditions has been evaluated.

Among different available computational methods to deal with such complex and nonlinear calculations, artificial neural networks (ANNs) have a proven record for highly accurate prediction of various material properties (Ref 29-32). As a powerful statistical tool, ANNs act such as the human nervous systems by implementing a logical model based on parallel interconnections of simple processing units (neurons) connected in a computing network to solve some kinds of elaborated modeling challenges like function estimation, classification and recognition of patterns (Ref 33, 34).

Recently, ANNs have also received increasing attention in some nondestructive applications. Implementing ANNs to predict failure strength of glass/epoxy composite laminates (Ref 34) and identification of the bond between concrete layers from acoustic emission parameters (Ref 35) are some of the new applications of artificial intelligence in the field of nondestructive evaluations.

ANNs were also used to determine the percentage of fibers embedded in a matrix of composite material using a vibration-based nondestructive test (Ref 36), automatic density prediction assuming lack of data on material composition by gamma-ray attenuation (Ref 37), efficient flaws detection in steel-welded joints combined with ultrasound testing (Ref 38), as well as active thermography for nonmetallic coating thickness prediction (Ref 39) and evaluation of weld joints to observe micro-gap by implementing magneto-optical imaging (Ref 40). Besides, in our recent work (Ref 41), we introduce an expert magnetic NDE

system using fuzzy logic approach for online characterization of DP steel microstructures with different martensite phase percentages. The results indicated that, even with the lack of data on applied frequency, simultaneously implementing multiple outputs enabled the NDE system to provide the accurate results only utilizing the specific Barkhausen noise outputs (position, width and height of the peaks).

The aim of this paper was to study the reliability of implementing the artificial intelligence approach in the simultaneous prediction of austenitizing and tempering temperatures of D2 tool steels. The experimental data derived from magnetic hysteresis loop outputs have been used for training and verifying the proposed ANN algorithm. Then, the efficiency of this new approach is examined in order to measure the ability of predicting more accurate results without prior knowledge about heat treating conditions.

2. Materials and Methods

D2 steel samples containing 1.5% C, 0.27% Mn, 0.2% Ni, 11.6% Cr, 0.32% Si, 0.63% Mo and 0.91% V (in weight percent) with dimensions of 100 mm × 21 mm × 4 mm were prepared for this work. Austenitizing treatment was done at five different temperatures for 30 min. Oil quenching and subsequent tempering was carried at six various temperatures for 2 h as indicated in Fig. 1. After polishing and etching of the heat-treated samples, the microstructures of the specimens were observed using SEM VP 1450. Besides, quantitative measurements of the retained austenite fraction were performed using x-ray diffractometry with monochromated Cu K α radiation.

Figure 2 presents the block scheme of the magnetic hysteresis measurement setup. To measure magnetic saturation (B_s), coercivity (H_c) and magnetic differential permeability (μ_{diff}), a U-shaped magnetizing coil made of Fe-Si-laminated core was used to apply a triangular waveform having a frequency of 5 Hz. It obtains a time-varying applied voltage, $V_1(t)$, in the driving coil which converts to the excitation field (H). To plot $B-H$ curves (hysteresis loops), the induced voltages recorded by a surrounding pick up coil of 500 turns, $V_2(t)$, were converted to density of magnetic flux (B) using Faraday's law of induction (Ref 42):

$$V_2(t) = -NS \frac{dB}{dt} \quad (\text{Eq 1})$$

where S and N are, respectively, the cross section of the sample and the number of pickup coil's turns. Plotting $B-H$ curve, differential permeability curve has been obtained using Eq 2:

$$\mu_{diff} = \frac{1}{\mu_0} \frac{dB}{dH} \quad (\text{Eq 2})$$

where μ_0 is $4\pi \times 10^{-7}$ Henry/m. Plotting the μ_{diff} changes versus H , one can consider the changes in maximum μ_{diff} as one of the measured magnetic outputs. The information extracted from the $B-H$ loops was then acquired using a digital oscilloscope and stored in a computer for further data processing. Finally, a MATLAB script was used for processing data.

The $B-H$ information was put into the ANN structure in terms of B_s , H_c and maximum μ_{diff} , bearing in mind the effect of different austenitizing and tempering temperatures as the

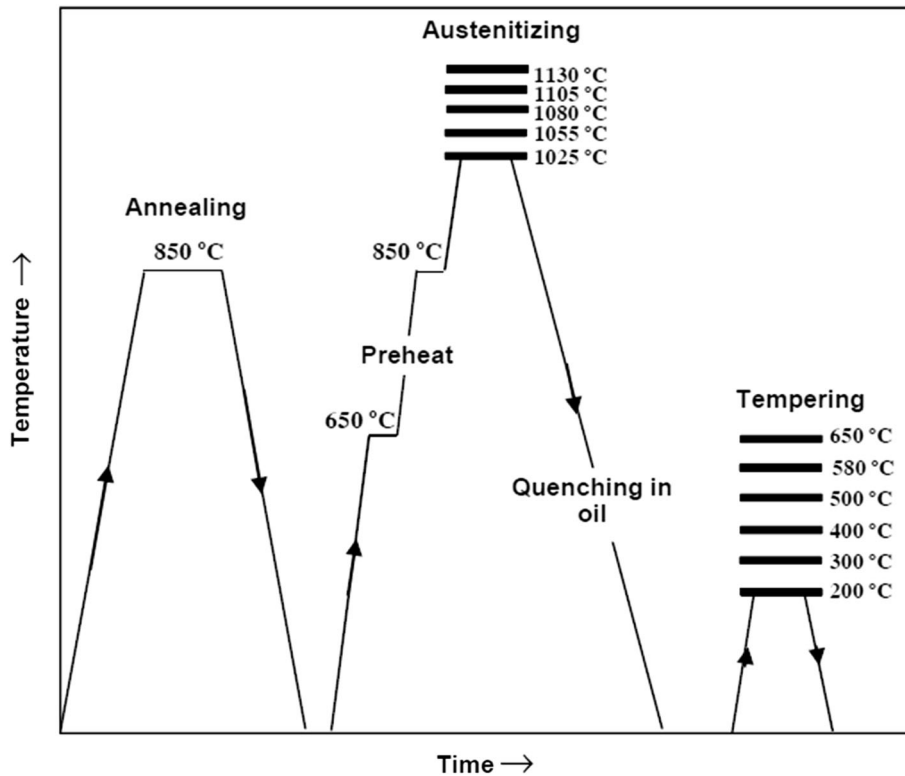


Fig. 1 Heat treatment procedures

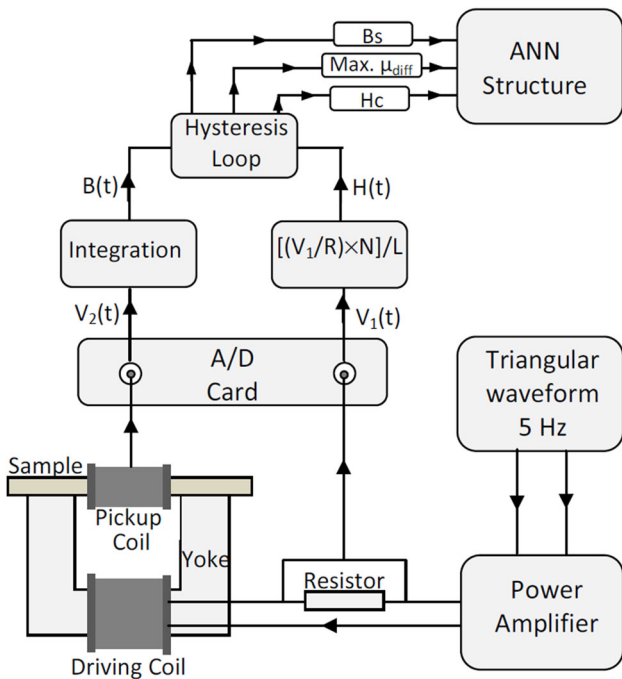


Fig. 2 Schematic illustrations for B-H measurement system

system outputs. Figure 3 shows the used framework of the ANN consisting of four different layers. Having some nodes, every layer generates outputs as the inputs for the next layer. A multiple layer network with feed-forward back-propagation

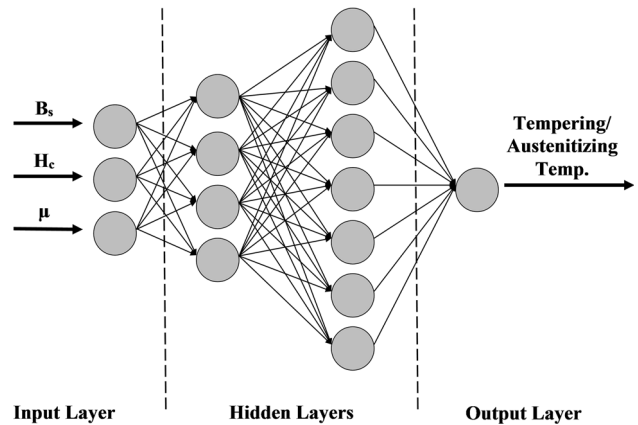


Fig. 3 The proposed ANN structure used for nondestructive modeling

(FFBPN) algorithm was used in the present paper as the most popular training algorithm in supervised networks. Feed-forward neural network usually consists of some hidden layers and their nodes to allow them dealing with nonlinear and complex tasks. The most significant affecting parameter in the performance of the used network is to find suitable numbers of the hidden layers and their nodes. There is not any specific trend or rule for the selection of suitable numbers of them, but these selections significantly depend upon the analyzer's experience and the problem's nature (Ref 43). In FFBPN algorithm, the initial weights are randomly chosen; then, inputs pass through the neural network and eventually outputs are compared with desired values considering errors (Ref 34, 43, 44).

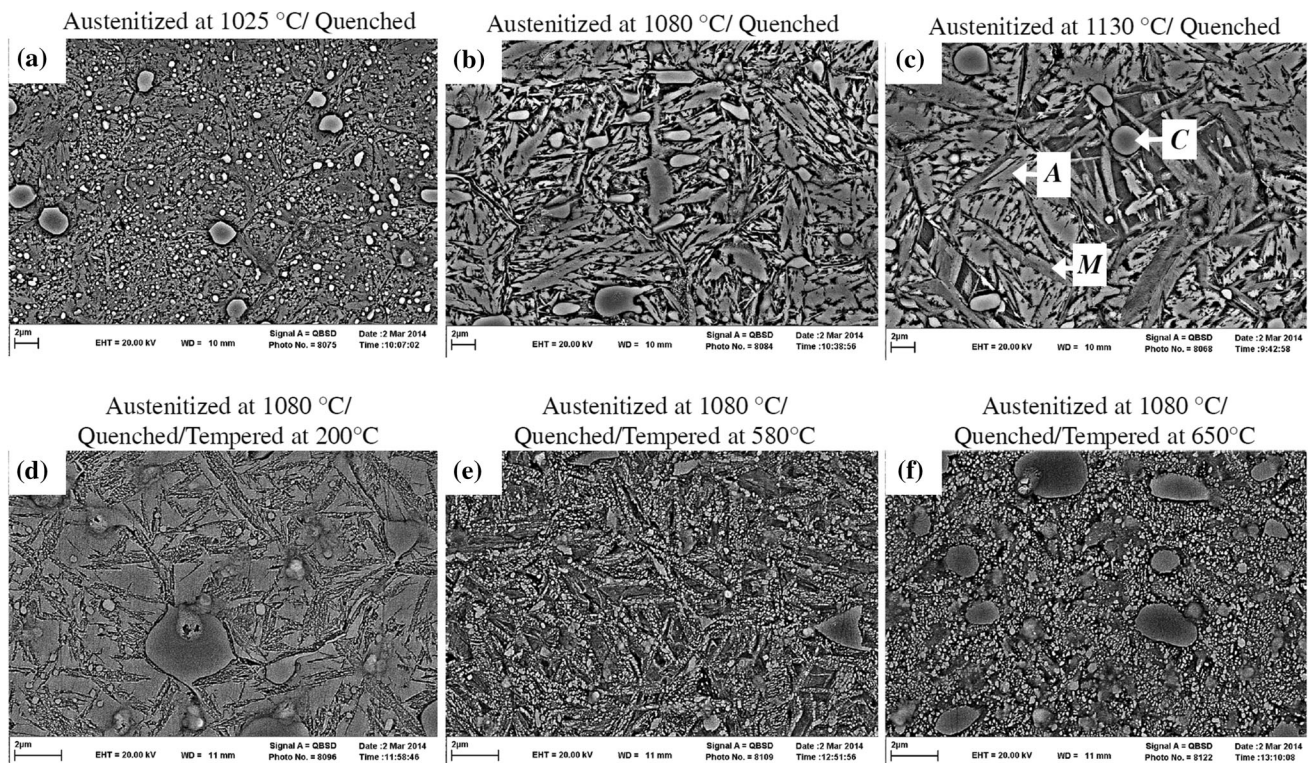


Fig. 4 SEM images of the austenitized steels at (a) 1025 °C, (b) 1080 °C and (c) 1130 °C which were quenched in oil and the steels austenitized at 1080 °C/quenched and tempered at (d) 200 °C, (e) 580 °C, and (f) 650 °C. Etched with Vilella

Table 1 Quantitative values of alloying elements dissolved in austenite phase at various temperatures obtained using Thermo-Calc software

Austenitizing temperature, °C	1000	1025	1055	1080	1105	1130
Amount of alloying elements dissolved in austenite phase, wt.%						
C	0.500	0.530	0.610	0.670	0.740	0.815
Cr	6.100	6.250	6.750	7.200	7.650	8.050
Mo	0.410	0.435	0.470	0.495	0.515	0.535
V	0.115	0.160	0.210	0.245	0.290	0.320

3. Results and Discussion

Figure 4(a), (b), and (c) corresponds to micrographs of the as-quenched state obtained by austenitizing at 1025, 1080 and 1130 °C, respectively. Martensite (M), undissolved carbides (C) and retained austenite (A) are phases that observe in the microstructures. As indicated in Fig. 4, increase in austenitizing temperature makes the microstructure coarser and the martensite plates surrounded by the austenite phase are more apparent. Besides, a lower fraction of undissolved carbides is observed in the matrix of the sample austenitized at higher temperatures. The main change is attributed to the retained austenite fraction that has increased with increasing austenitizing temperature. Qualitatively, a higher fraction of bright and smooth surfaces, which represents the retained austenite phase, is seen in Fig. 4 (c) compared to Fig. 4(a). The main reason for retained austenite enhancement is due to the higher solubility of alloy carbides (chrome, molybdenum and vanadium carbides) at higher temperatures. Table 1 shows the amounts of alloying elements dissolved in austenite phase at various temperatures calculated by Thermo-Calc software TCFE0 steels/Fe alloys

database version. As the table presented, dissolution of carbon and alloy elements into the austenitic lattice (at high temperature) increases with austenitizing temperature. Increase in austenitizing temperature from 1025 to 1130 °C increases the weight percentage of carbon, chrome, molybdenum and vanadium dissolved in austenite from 0.530 to 0.815, 6.250 to 8.050, 0.435 to 0.535, and 0.160 to 0.320, respectively. These significant changes in dissolution lead to a noticeable reduction in martensite start temperature [from 220 °C to 90 °C with the austenitizing temperature of 1025 to 1130 °C, respectively (Ref 45)] and, consequently, increase the amount of retained austenite. Thus, the amounts of dissolved carbides as well as subsequent retained austenite are strongly dependent on the austenitizing temperature (Ref 22).

Figure 4(d), (e), and (f) shows representative micrographs for the samples tempered at 200, 580, and 650 °C (with austenitizing temperature of 1080 °C). Figure 4(d) illustrates the tempered microstructure at 200 °C, which has transition carbides formed from the martensite plates. In the sample tempered at 580 °C (Fig. 4e), carbides are precipitated all over the matrix, implying the disintegration of the retained austenite. In this case, the microstructure has revealed the

carbide particles distributed in the ferrite matrix. Figure 4(f) indicates that with an increase in the tempering temperature up to 650 °C, the precipitated carbides are changed to spheroidized form. By comparing the integrated intensity (area under the peak above the background) of x-ray diffraction peaks of the austenite phase with martensite one, the percentage of retained austenite is assessed quantitatively. This is due to the fact that the total integrated intensity of all diffraction peaks for austenite or martensite phase is proportional to the volume fraction (Ref 46). The details of calculations can be found elsewhere (Ref 8, 22). Calculated results of the retained austenite for quenched samples

presented in Table 2 indicate the significant variations of the retained austenite percentage from 20.55 to 42.0% with the rise in the austenitizing temperature from 1025 to 1130 °C, respectively.

The retained austenite percentages in the samples austenitized at 1080 °C and tempered in the range 200-650 °C are also presented in Table 2. The amount of the retained austenite is constant at the initial temperatures (up to 300 °C), decreases slightly at 400 °C, followed by a significant decrease at 500 °C, and finally, disappears at samples tempered at 580 °C and 650 °C. This means that the retained austenite decomposition during the tempering starts at about 400 °C and ends at 580 °C.

Table 2 Quantitative XRD measurements of retained austenite percentage for the samples with different austenitizing and tempering treatments

Quenched samples						
Austenitizing temperature	1025	1055	1080	1105	1130	
Retained austenite %	20.55	24.18	33.00	39.82	42.00	
Austenitized at 1080 °C/quenched/tempered samples						
Tempering temperature	200	300	400	500	580	650
Retained austenite %	32.70	32.20	28.24	16.35	4.35	3.50

Table 3 Conditions of heat treatments and the corresponding nondestructive test results used for constructing ANN model

Test run	Austenitizing temperature, °C	Tempering temperature, °C	B_s	H_c	Maximum μ_{diff}
1	1025	25	0.525	1637	1215
2	1025	200	0.540	1612	1236
3	1025	300	0.545	1608	1240
4	1025	400	0.585	1579	1282
5	1025	500	0.615	1568	1305
6	1025	580	0.930	1445	2295
7	1025	650	1.450	1268	3080
8	1055	25	0.390	1784	1049
9	1055	200	0.415	1773	1054
10	1055	300	0.420	1770	1065
11	1055	400	0.480	1726	1170
12	1055	500	0.495	1718	1167
13	1055	580	0.831	1507	2290
14	1055	650	1.414	1277	3050
15	1080	25	0.338	1841	936
16	1080	200	0.375	1820	953
17	1080	300	0.385	1818	976
18	1080	400	0.460	1764	1110
19	1080	500	0.480	1752	1101
20	1080	580	0.772	1560	2095
21	1080	650	1.378	1315	3039
22	1105	25	0.285	1914	694
23	1105	200	0.320	1870	810
24	1105	300	0.330	1862	820
25	1105	400	0.390	1830	893
26	1105	500	0.420	1833	926
27	1105	580	0.556	1740	1580
28	1105	650	1.306	1348	2950
29	1130	25	0.194	2057	567
30	1130	200	0.240	2012	594
31	1130	300	0.245	2007	610
32	1130	400	0.310	1972	720
33	1130	500	0.320	1955	758
34	1130	580	0.430	1900	1350
35	1130	650	1.260	1380	2850

Applying the hysteresis loop method, magnetic saturation (B_s), maximum differential permeability (μ_{diff}) and coercivity (H_c) are measured for samples tabulated in Table 3 and the results are presented in Fig. 5. Figure 5(a) and (b) show that B_s and maximum μ_{diff} decrease with the rise in the austenitizing temperature for as-quenched samples. This can be due to the increasing of paramagnetic retained austenite (from 20.55 to 42.00%) as a result of increasing in austenitizing temperature. On the other hand, as Fig. 5(c) shows, H_c exhibits an opposite increasing trend with austenitizing temperature. This is attributed to the presence of higher retained austenite fraction at elevated austenitizing temperatures which provide more pinning sites against the domain wall motion in the magnetizing process. The reduction in magnetic saturation and increase in coercivity as a result of the retained austenite formation is consistent with the results reported for the formation of reverted austenite phase during aging of maraging 350 steel (Ref 47).

In the case of tempering treatment, for various austenitizing temperatures, the variation trends of B_s , maximum μ_{diff} and coercivity with tempering temperatures are similar. The B_s and maximum μ_{diff} values increase while H_c values decrease slightly with tempering at 200 °C and 300 °C as a result of reduction in tetragonality of martensite and formation of transition carbides (ϵ -carbides) (Ref 8). Afterward, there is an upward tendency for B_s and maximum μ_{diff} and a small downward trend for H_c at 400 °C, which is due to further reduction in dislocation density as well as decomposition of retained austenite initiated at 300-400 °C (Fig. 5).

In the following, the nearly constant values are observed for all the outputs in the range 400-500 °C. This is related to manifestation of two completely different effects [decomposition of retained austenite (Table 2) versus precipitation of secondary carbides (Ref 7, 8)] on the domain walls motion in the magnetization process. Finally, a continuous sharp increase for B_s and maximum μ_{diff} and a decrease for H_c can be seen with increasing temperature (Fig. 5). As the disintegration of retained austenite completes, the clear changes in the output values are due to the formation of ferrite from austenite decomposition which has a fast and high-grade reflex under the excited field in comparison with nonmagnetic retained austenite and the hard magnetically martensite phases. Since the decomposition of retained austenite completes at around 580 °C, spheroidization of carbides (as shown in Fig. 4f) has a dominant effect on the magnetic parameters (Ref 8). Indeed, the change in carbide morphology, from coarse lamellar to disperse spherical, increases mean free path of the domain walls displacement and facilitates the magnetization process (Ref 48).

For samples austenitized at other temperatures (1025, 1050, 1105 and 1130 °C), variations of B_s , maximum μ_{diff} and H_c versus tempering temperature, demonstrate a similar pattern. The higher values of retained austenite fraction at higher austenitizing temperatures are an only reason to explain the difference between the $B-H$ outputs in Fig. 5.

Considering the relationships between magnetic parameters and tempering temperatures for different austenitizing temperatures (Fig. 5), traditionally, the austenitizing temperature

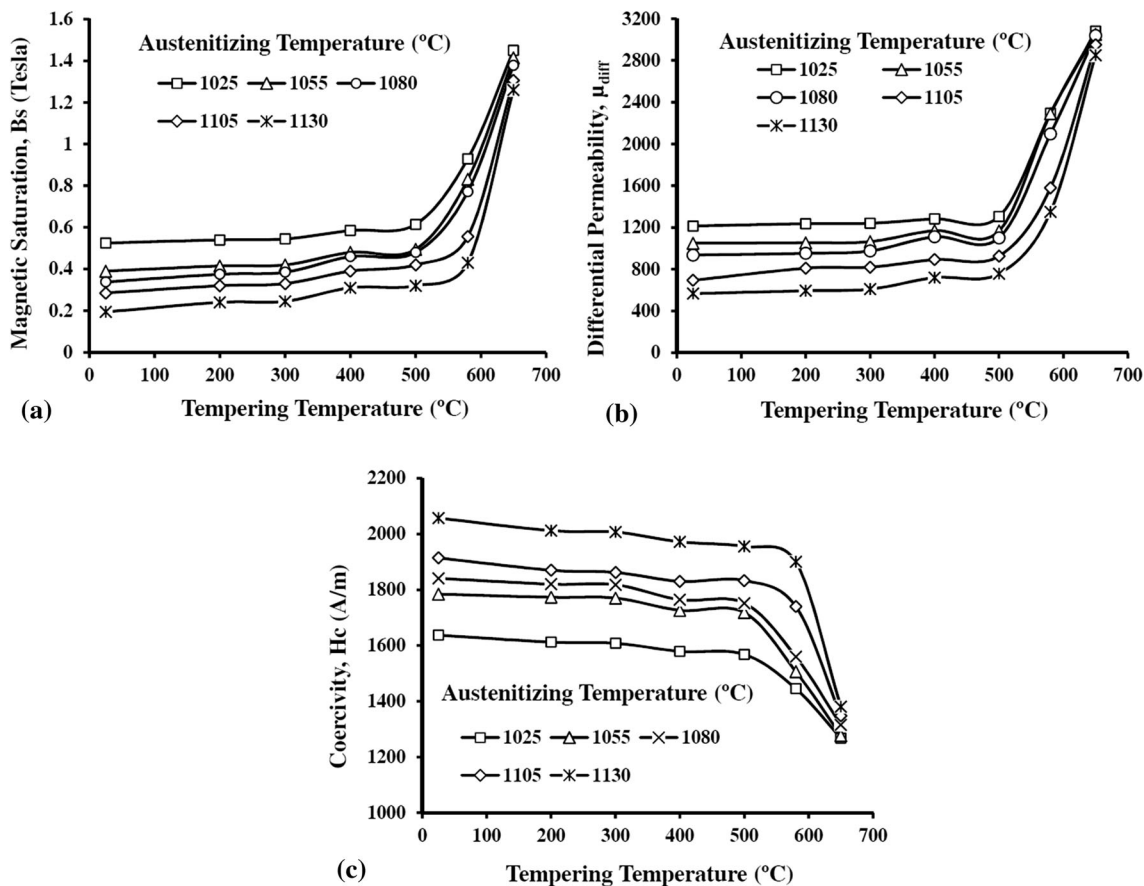


Fig. 5 Variations of (a) B_s , (b) maximum μ_{diff} , and (c) H_c , for the austenitized samples at 1025-1130 °C and tempered at 200-650 °C

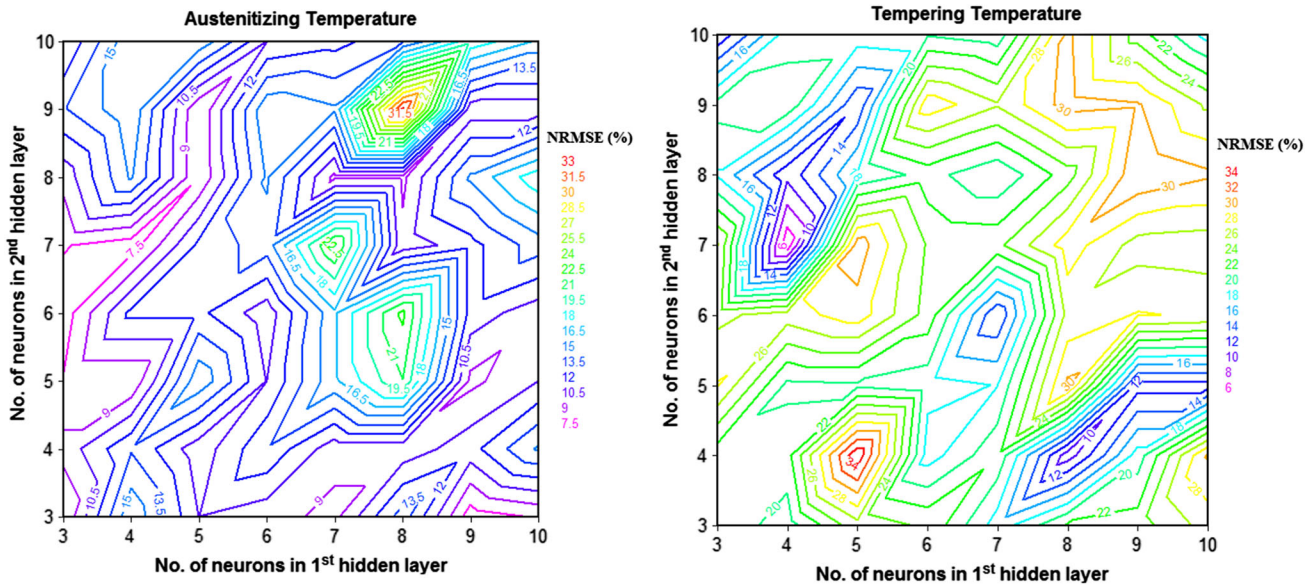


Fig. 6 Finding the best numbers of the nodes in the first and second hidden layers

Table 4 ANN training parameters

Neural network settings	Value/type
Network type	FFBPN
Training algorithm	Levenberg–Marquardt
First hidden layer	4 neurons (Tansig transfer functions)
Second hidden layer	7 neurons (Tansig transfer functions)
Final layer	1 neuron (Purelin transfer function)
Achievement function	MSE
Epoch No.	150
Max fail	45
Min grad	1×10^{-10}
Mu	0.005
Mu inc	10
Mu dec	0.1
Mu max	1×10^{10}

should be considered constant to determine tempering temperature. In other words, if the austenitizing temperature is not given, nondestructive determination of tempering temperature could not be possible. To overcome this limitation here, the ANN was applied on all the magnetic parameters to detect the austenitizing and tempering temperatures of AISI D2 parts with unknown heat treatment conditions.

Modeling the biological neural system of human beings, ANN is capable of implementing the ability to learn as the most important feature of the brain. For this purpose, the database presented in Table 3 is divided into three sets. Training, validation and testing sets are, respectively, used for adjusting the errors and weights in a network, editing ANN structure and evaluating the network's performance while facing new data (Ref 49, 50). Numbers of 30 and 28 test results are fed into the network for training and validation processes to predict the austenitizing and tempering temperatures, respectively.

Prior to calculation, all input data are normalized to improve the sensitivity and accuracy of the network but at the outputs of the calculations are denormalized to achieve actual output and error values (Ref 43, 51). In the present study, $X(N)$ can be

calculated as the normalized input value for introducing into the ANN structure using the formula $X(N) = [X(\text{Actl}) - X(M)] / X(\text{SD})$ (where $X(\text{Actl})$ is the actual value and, $X(M)$ and $X(\text{SD})$ are, respectively, the mean and standard deviation of all actual parameters). Using the above equation, $X(N)$ can be calculated as the normalized input value for introducing into the ANN structure.

Using learning database to train the networks, some ANN structures were evaluated while their number of hidden layers and constituent neurons were changed. According to preliminary finding the mean square error (MSE) with the lowest value (Fig. 6), network structure consisting of two hidden layers (four nodes for layer one and seven nodes for layer two) is implemented as previously shown in Fig. 3.

Unwanted problems such as overfitting, overtraining and memorization take place as the results of potent pattern-recognition capabilities of ANN during calibration of neural networks. This difficulty happens when the network has large architecture as it starts to memorize data instead of trend recognition. On the other hand, poor accuracy of the neural network predictions may occur as a result of smaller architecture and database (Ref 52). Also, there is a risk of poor training performance in the case of ANNs implementing too few neurons in each of the layers (Ref 50). Offsetting this unwanted problem, two measures were used: cross-validation and choosing a reasonable enough number of layers and neurons.

ANN training parameters used ultimately for this study are presented in Table 4. To attain the least error surface, a supervised feed-forward learning framework based on Levenberg–Marquardt back-propagation algorithm is used, and then, across plots of the testing predictions is utilized to assess network performance by the highest possible prediction accuracy. In the used back-propagation algorithm, the nondestructive data are fed into the input layer, then pass through the hidden layers, and finally they reach the output layer (Fig. 3). If there is difference between the expected and actual values in the output layer, the error passes backwards to the input layer through the hidden layers during the learning and training. Consequently, the error signal spreads to all input neurons and

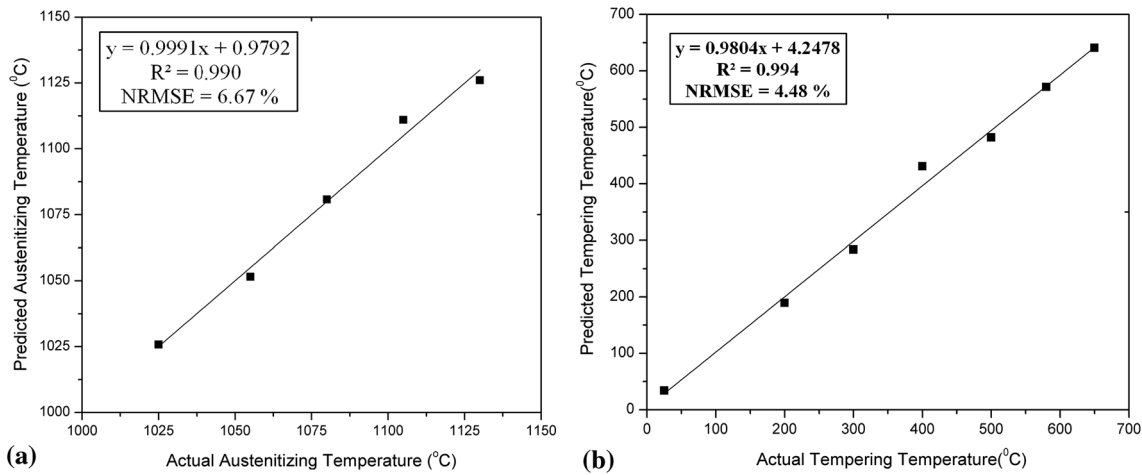


Fig. 7 ANN-predicted data vs. experimental data for testing data sets: (a) austenitizing temperature and (b) tempering temperature

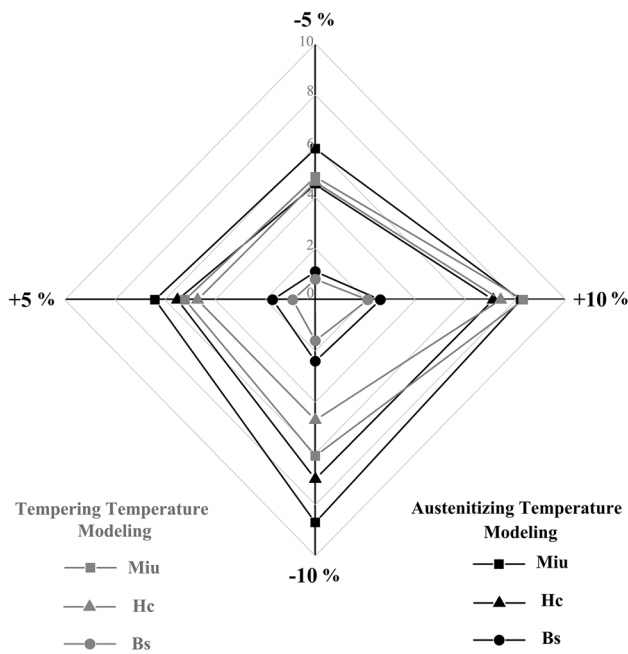


Fig. 8 Impact of the ANN's inputs (nondestructive testing outputs) on detection of austenitizing/tempering temperatures

acts as a weight modification for each input. Adjusting the weights, a new cycle starts passing forward the nondestructive data from input layer to output layer. This procedure continues until reaching an acceptable level of error or it can be terminated after completion of a specified number of learning cycles (Ref 53-56). In both hidden layers, tan-sigmoid transfer functions are used. Implementing this function for hidden layers is due to obtaining an effective improvement in the input-output relation when a small variation in updated weights takes place. In the output layer, finally, a linear purlin transfer function was utilized to produce output of network in the specific range of -1 to 1 .

Training of the network lasts until the specified mean square error and epochs are reached. Finally, a testing data set is introduced to the proposed ANN model for testing the

performance and efficiency of the training procedures. For tempering temperatures prediction, unseen test runs: 4, 9, 14, 17, 22, 26, and 34 were introduced to the neural network. Also for austenitizing temperatures prediction, test runs: 7, 14, 21, 28, and 35 were evaluated. Testing databases are used to estimate the performance of the network and its potential to predict both temperatures when facing unobserved situations as well. To assess the achievements of network in prediction of the results, both normalized error of root mean square (NRMSE) and determination's coefficient (R^2) are calculated. Figure 7 represents regression graphs for prediction of austenitizing and tempering temperatures of D2 steels using the proposed model. As can be clearly seen, the act of modeling is acceptable for unseen test data on the whole (Fig. 7). Evaluating the task of modeling, ANN revealed the best prediction results, namely the lowest NRMSE and the highest R^2 values. The predicted and experimental values are quite the same for $R^2=1.0$; on the other hand, small values for NRMSE indicate how close the predicted and experimental data are.

Based on the findings, the used back-propagation algorithm was able to model the nonlinear and complex relationships between the inputs and outputs to provide the nonlinear mapping. To study the sensitivity of the proposed ANN's responses to the variations of the inputs, the sensitivity analysis was conducted. The sensitivity analysis can measure the significance and impact of each of the nondestructive testing outputs on the tempering and austenitizing temperature modeling. Monitoring the sensitivity of the ANN's responses, each inputs varied by the rates of 5 and 10 and the resulting output changes (provided by the proposed ANN model) are calculated using Eq 3 (Ref 52).

$$\text{Sensitivity of input parameter (\%)} = \frac{1}{n} \sum_{k=1}^n \left(\frac{\text{Variation of output (\%)}}{\text{Variation of input (\%)}} \right) \quad (\text{Eq 3})$$

where n is the number of data points.

Figure 8 shows the results of the sensitivity analysis. All axes were gridded from 0 to 10 in steps of 2%. According to the results, the B_s output has comparatively less influence on detection of austenitizing/tempering temperatures compared to maximum μ_{diff} and H_c outputs.

Table 5 The hardness values extracted from (Ref 54), as a function of actual/predicted austenitizing and tempering temperatures

Test run	Austenitizing temperature, °C	Tempering temperature, °C	Hardness (RC) from (Ref 54)
4			
Actual	1025.0	400.0	58.7
Predicted	1029.1	431.0	59.1
14			
Actual	1055.0	650.0	41.8
Predicted	1051.5	640.8	40.9
17			
Actual	1080.0	300.0	57.2
Predicted	1095.4	283.7	57.5
21			
Actual	1080.0	650.0	40.2
Predicted	1080.8	660.4	39.3
26			
Actual	1105.0	500.0	57.2
Predicted	1098.8	482.2	58.0

The proposed ANN model obviously reveals the successful introducing of the artificial intelligence to a magnetic nondestructive evaluation system for D2 steel parts. It is able to accurately predict austenitizing and tempering temperatures as a function of BH testing outputs. The successful performance of the ANN applied on all the magnetic outputs data is attributed to detect the austenitizing/tempering temperatures of AISI D2 parts with unknown heat treatment conditions, simultaneously.

Based on the relations established in the literature (Ref 57), the hardness values of D2 steel can be obtained using austenitizing and tempering temperatures. The hardness values were determined for five random samples of the present study and are tabulated in Table 5, which show an excellent agreement between the actual and predicted results. This comparison highlights the benefits of implementing the ANN to predict the heat treatment conditions which have a great impact on the mechanical properties of this type of steel.

4. Conclusion

In this study, an advanced application of artificial intelligence for simultaneous nondestructive evaluation of austenitizing and tempering temperatures of D2 tool steels is evaluated based on magnetic hysteresis method.

Based on the results, magnetic hysteresis method reveals great sensitivity to microstructural changes of the AISI D2 tool steel during heat treating process. Variations of austenitizing temperatures affect phase fraction of retained austenite, which, in turn, results in changing the magnetic response of the steel. As a result of tempering, microstructural changes lead to variations of electromagnetic parameters. ϵ carbides and cementite precipitations, decomposition of retained austenite, the exhibition of secondary hardening, as well as carbide spheroidization are effective changes which alter B_s , maximum μ_{diff} and H_c .

To simultaneously accurate predictions of tempering and austenitizing temperatures, present paper implements the benefits of ANN modeling for reliable processing of BH outputs. Feeding multiple BH outputs, it is possible for the artificial neural network to make an advance in providing the most accurate outcomes using only B_s , maximum μ_{diff} and H_c .

Taking into account unseen data sets, high calculated R^2 and low NRMSE values confirm the successful application of ANN to predict both austenitizing and tempering temperatures. The modeled austenitizing temperatures are obtained without knowing the values of tempering temperatures, and vice versa. The results of the BH nondestructive testing coupled to artificial intelligence modeling can be a key consideration for choosing this reliable expert NDE technique to predict heat treatment conditions for the industrial assessment of D2 tool steels.

Acknowledgment

The authors would like to thank Professor David Galloway, from the University of Melbourne, Australia, for his comments on editing the manuscript.

References

1. G.A. Roberts, R. Kennedy, and G. Krauss, *Tool Steels*, 5th ed., ASM International, Materials Park, 1998
2. P.M. Uterweiser, *Heat Treater's Guide, Standard Practices and Procedures for Steel*, American Society for Metals, Cleveland, 1989
3. S. Kahrobaee and M. Kashefi, Microstructural Characterization of Quenched AISI, D2 Tool Steel Using Magnetic/Electromagnetic Nondestructive Techniques, *IEEE Trans. Magn.*, 2015, **51**(9), p 1–7
4. Y. Hirotsu and S. Nagakura, Crystal Structure and Morphology of the Carbide Precipitated From Martensitic High Carbon Steel During the First Stage of Tempering, *Acta Metal.*, 1972, **20**(4), p 645–655
5. V.G. Gavriljuk, V.A. Sirosh, Y.N. Petrov, A.I. Tyshchenko, W. Theisen, and A. Kortmann, Carbide Precipitation During Tempering of a Tool Steel Subjected to Deep Cryogenic Treatment, *Metal. Mater. Trans. A*, 2014, **45**(5), p 2453–2465
6. A. Kokosza and J. Pacyna, Evaluation of Retained Austenite Stability in Heat Treated Cold Work Tool Steel, *J. Mater. Process. Technol.*, 2005, **162–163**, p 327–331
7. P. Bała, J. Pacyna, and J. Krawczyk, The Influence of The Kinetics of Phase Transformations During Tempering on the Structure Development in a High Carbon Steel, *Arch. Metall. Mater.*, 2007, **52**(1), p 113–120
8. S. Kahrobaee and M. Kashefi, Electromagnetic Nondestructive Evaluation of Tempering Process in AISI, D2 Tool Steel, *J. Magn. Magn. Mater.*, 2015, **382**, p 359–365
9. S. Ding, G.Y. Tian, G. Dobmann, and P. Wang, Analysis of Domain Wall Dynamics Based on Skewness of Magnetic Barkhausen Noise for

- Applied Stress Determination, *J. Magn. Magn. Mater.*, 2017, **421**, p 225–229
10. A. Freddy, F. Grijalba, and L.R. Padovese, Non-destructive Scanning for Applied Stress by the Continuous Magnetic Barkhausen Noise Method, *J. Magn. Magn. Mater.*, 2018, **446**, p 231–238
 11. O. Kyprijs, I.C. Nlebedim, and D.C. Jiles, Measuring Stress Variation with Depth Using Barkhausen Signals, *J. Magn. Magn. Mater.*, 2016, **407**, p 377–395
 12. J. Pala and J. Bydzovsky, Barkhausen Noise as a Function of Grain Size in Non-oriented FeSi Steel, *Measurement*, 2013, **46**, p 866–870
 13. L. Batista, U. Rabe, I. Altpeter, S. Hirsekorn, and G. Dobmann, On the Mechanism of Nondestructive Evaluation of Cementite Content in Steels Using a Combination of Magnetic Barkhausen Noise and Magnetic Force Microscopy Techniques, *J. Magn. Magn. Mater.*, 2014, **354**, p 248–256
 14. J.W. Wilson and G.Y. Tian, Pulsed Electromagnetic Methods for Defect Detection and Characterization, *NDT E Int.*, 2007, **40**, p 275–283
 15. A. Martinez-de-Guerenu, K. Gurruchaga, and F. Arizti, Nondestructive Characterization of Recovery and Recrystallization in Cold Rolled Low Carbon Steel by Magnetic Hysteresis Loops, *J. Magn. Magn. Mater.*, 2007, **316**, p e842–e845
 16. C.S. Angani, D.G. Park, C.G. Kim, P. Leela, P. Kollu, and Y.M. Cheong, The Pulsed Eddy Current Differential Probe to Detect a Thickness Variation in an Insulated Stainless Steel, *J. Nondestruct. Eval.*, 2010, **29**, p 248–252
 17. D. Park, C. Sekar Angani, B.P.C. Rao, G. Vértesy, D.-H. Lee, and K.-H. Kim, Detection of the Subsurface Cracks in a Stainless Steel Plate Using Pulsed Eddy Current, *J. Nondestruct. Eval.*, 2013, **32**, p 350–353
 18. M. Sheikh Amiri and M. Kashefi, Investigation of Variables Affecting Impedance Plane in Eddy Current Testing of Carburized Steels, *J. Mater. Eng. Perform.*, 2011, **20**, p 476–480
 19. X.J. Hao, W. Yin, M. Strangwood, A.J. Peyton, P.F. Morris, and C.L. Davis, Off-Line Measurement of Decarburization of Steels Using a Multifrequency Electromagnetic Sensor, *Scripta Mater.*, 2008, **58**, p 1033–1036
 20. M. Sheikh Amiri and M. Kashefi, Application of Eddy Current Nondestructive Method for Determination of Surface Carbon Content in Carburized Steels, *NDT E Int.*, 2009, **42**(7), p 618–621
 21. K. Davut and C. Hakan Gür, Monitoring the Microstructural Changes During Tempering of Quenched SAE 5140 steel by Magnetic Barkhausen Noise, *J. Nondestruct. Eval.*, 2007, **26**(2), p 107–113
 22. S. Kahrobaee and M. Kashefi, Assessment of Retained Austenite in AISI, D2 Tool Steel Using Magnetic Hysteresis and Barkhausen Noise Parameters, *J. Mater. Eng. Perform.*, 2015, **24**(3), p 1192–1198
 23. M. Kashefi, A. Rafsanjani, S. Kahrobaee, and M. Alaei, Magnetic Nondestructive Technology for Detection of Tempered Martensite Embrittlement, *J. Magn. Magn. Mater.*, 2012, **324**(23), p 4090–4093
 24. K.V. Rajkumar, S. Vaidyanathan, A. Kumar, T. Jayakumar, B. Raj, and K.K. Ray, Characterization of Aging-Induced Microstructural Changes in M250 Maraging Steel Using Magnetic Parameters, *J. Magn. Magn. Mater.*, 2007, **312**(2), p 359–365
 25. K. Rajkumar, B. Rao, B. Sasi, A. Kumar, T. Jayakumar, B. Raj, and K. Ray, Characterization of Aging Behaviour in M250 Grade Maraging Steel Using Eddy Current Non-destructive Methodology, *Mater. Sci. Eng. A*, 2007, **464**(1–2), p 233–240
 26. S. Ghanei, M. Kashefi, and M. Mazinani, Eddy Current Nondestructive Evaluation of Dual Phase Steel, *Mater. Des.*, 2013, **50**, p 491–496
 27. S. Ghanei, M. Kashefi, and M. Mazinani, Comparative Study of Eddy Current and Barkhausen Noise Nondestructive Testing Methods in Microstructural Examination of Ferrite–Martensite Dual-Phase Steel, *J. Magn. Magn. Mater.*, 2014, **356**, p 103–110
 28. S. Ghanei, A. Saheb Alam, M. Kashefi, and M. Mazinani, Non-destructive Characterization of Microstructure and Mechanical Properties of Intercritically Annealed Dual-Phase Steel by Magnetic Barkhausen Noise Technique, *Mater. Sci. Eng. A*, 2014, **607**, p 253–260
 29. M. Zare and J. Vahdati Khaki, Prediction of Mechanical Properties of a Warm Compacted Molybdenum Prealloy Using Artificial Neural Network and Adaptive Neuro-Fuzzy Models, *Mater. Des.*, 2012, **38**, p 26–31
 30. S.J. Farley, J.F. Durodola, N.A. Fellows, and L.H. Hernández-Gómez, High Resolution Non-destructive Evaluation of Defects Using Artificial Neural Networks and Wavelets, *NDT E Int.*, 2012, **52**, p 69–75
 31. P.B. García-Allende, J. Mirapeix, O.M. Conde, A. Cobo, and J.M. López-Higuera, Spectral Processing Technique Based on Feature Selection and Artificial Neural Networks for Arc-Welding Quality Monitoring, *NDT E Int.*, 2009, **42**(1), p 56–63
 32. G.-Z. Quan, T. Wang, Y.-I. Li, Z.-Y. Zhan, and Y.-F. Xia, Artificial Neural Network Modeling to Evaluate the Dynamic Flow Stress of 7050 Aluminum Alloy, *J. Mater. Eng. Perform.*, 2016, **25**(2), p 553–564
 33. A. Das, J. Maiti, and R.N. Banerjee, Process Control Strategies for a Steel Making Furnace Using ANN with Bayesian Regularization and ANFIS, *Expert Syst. Appl.*, 2010, **37**(2), p 1075–1085
 34. C. Suresh Kumar, V. Arumugam, R. Sengottuvelusamy, S. Srinivasan, and H.N. Dhakal, Failure Strength Prediction of Glass/Epoxy Composite Laminates from Acoustic Emission Parameters Using Artificial Neural Network, *Appl. Acoust.*, 2017, **115**, p 32–41
 35. Ł. Sadowski, J. Hola, and S. Czarnecki, Non-destructive Neural Identification of the Bond Between Concrete Layers in Existing Elements, *Constr. Build. Mater.*, 2016, **127**, p 49–58
 36. N.I.E. Farhana, M.S. Abdul Majid, M.P. Paulraj, E. Ahmadhilmilmi, M.N. Fakhzan, and A.G. Gibson, A Novel Vibration Based Non-destructive Testing for Predicting Glass Fibre/Matrix Volume Fraction in Composites Using a Neural Network Model, *Compos. Struct.*, 2016, **144**, p 96–107
 37. C.M. Salgado, L.E.B. Brandão, C.C. Conti, and W.L. Salgado, Density Prediction for Petroleum and Derivatives by Gamma-Ray Attenuation and Artificial Neural Networks, *Appl. Radiat. Isot.*, 2016, **116**, p 143–149
 38. F.C. Cruz, E.F. Simas Filho, M.C.S. Albuquerque, I.C. Silva, C.T.T. Farias, and L.L. Gouvêa, Efficient Feature Selection for Neural Network Based Detection of Flaws in Steel Welded Joints Using Ultrasound Testing, *Ultrasonics*, 2017, **73**, p 1–8
 39. H. Wang, S.-J. Hsieh, B. Peng, and X. Zhou, Non-metallic Coating Thickness Prediction Using Artificial Neural Network and Support Vector Machine with Time Resolved Thermography, *Infrared Phys. Technol.*, 2016, **77**, p 316–324
 40. X. Gao, Y. Chen, D. You, Z. Xiao, and X. Chen, Detection of Micro Gap Weld Joint by Using Magneto-Optical Imaging and Kalman Filtering Compensated With RBF Neural Network, *Mech. Syst. Signal. Process.*, 2017, **84**(Part A), p 570–583
 41. S. Ghanei, H. Vafaenezhad, M. Kashefi, A.R. Eivani, and M. Mazinani, Design of an Expert System Based on Neuro-Fuzzy Inference Analyzer for On-Line Microstructural Characterization Using Magnetic NDT Method, *J. Magn. Magn. Mater.*, 2015, **379**, p 131–136
 42. O. Stupakov, Investigation of Applicability of Extrapolation Method for Sample Field Determination in Single-Yoke Measuring Setup, *J. Magn. Magn. Mater.*, 2006, **307**(2), p 279–287
 43. H. Vafaenezhad, S. Ghanei, S.H. Seyedein, H. Beygi, and M. Mazinani, Process Control Strategies for Dual-Phase Steel Manufacturing Using ANN and ANFIS, *J. Mater. Eng. Perform.*, 2014, **23**(11), p 3975–3983
 44. G. Kranthi and A. Satapathy, Evaluation and Prediction of Wear Response of Pine Wood Dust Filled Epoxy Composites Using Neural Computation, *Comput. Mater. Sci.*, 2010, **49**(3), p 609–614
 45. M. Kashefi and S. Kahrobaee, Determination of Martensite Start Temperature Using an Electromagnetic Nondestructive Technology, *J. Alloys Compd.*, 2017, **720**, p 478–482
 46. ASTM E975-00, Standard Practice for X-Ray Determination of Retained Austenite in Steel with Near Random Crystallographic Orientation, ASTM Book of Standards, Vol. 03.01, West Conshohocken, PA, 2004
 47. S.S.M. Tavares, H.F.G. Abreu, J.M. Neto, M.R. da Silva, and I. Popa, A Magnetic Study of the Maraging 350 Steel, *J. Magn. Magn. Mater.*, 2004, **272**, p 785–787
 48. K. Davut and C.H. Gür, Monitoring the Microstructural Evolution in Spheroidized Steels by Magnetic Barkhausen Noise Measurements, *J. Nondestruct. Eval.*, 2010, **29**(4), p 241–247
 49. H. Vafaenezhad, S. Asadolahpour, N. Nayeypashae, S. Seyedein, and M. Aboutalebi, Intelligent Use of Data to Optimize Compressive Strength of Cellulose-Derived Composites, *Appl. Soft Comput.*, 2016, **40**, p 594–602
 50. M. Dehnavi, H. Vafaenezhad, M. Khakzadi, N. Nayeypashae, and A. Eivani, Modelling and Prediction Impression Creep Behaviour of Al–Cu Cast Alloy, *Int. J. Cast Met. Res.*, 2017, **30**(2), p 70–80

51. S.A. Sani, G. Ebrahimi, H. Vafaenezhad, and A. Kiani-Rashid, Modeling of Hot Deformation Behavior and Prediction of Flow Stress in a Magnesium Alloy Using Constitutive Equation and Artificial Neural Network (ANN) Model, *J. Magnes. Alloys*, 2018, **6**(2), p 134–144
52. H. Vafaenezhad, S. Seyedein, M. Aboutalebi, and A. Eivani, Application of Constitutive Description and Integrated ANFIS—ICA Analysis to Predict Hot Deformation Behavior of Sn–5Sb Lead-Free Solder Alloy, *J. Alloys Compd.*, 2017, **697**, p 287–299
53. L. Shi, S. Lin, Y. Lu, L. Ye, and Y. Zhang, Artificial Neural Network Based Mechanical and Electrical Property Prediction of Engineered Cementitious Composites, *Constr. Build. Mater.*, 2018, **174**, p 667–674
54. H. Vafaenezhad, S. Seyedein, M. Aboutalebi, and A. Eivani, Incorporating the Johnson–Cook Constitutive Model and a Soft Computational Approach for Predicting the High-Temperature Flow Behavior of Sn–5Sb Solder Alloy: A Comparative Study for Processing Map Development, *J. Electron. Mater.*, 2017, **46**(1), p 467–477
55. P. Verpoort, P. MacDonald, and G.J. Conduit, Materials Data Validation and Imputation with an Artificial Neural Network, *Comput. Mater. Sci.*, 2018, **147**, p 176–185
56. Y. Xu and R. Jin, Measurement of Reinforcement Corrosion in Concrete Adopting Ultrasonic Tests and Artificial Neural Network, *Constr. Build. Mater.*, 2018, **177**, p 125–133
57. T.-H. Hejazi and S. Kahrobaee, A Predictive Model for Characterizing Hardness of D2 Tool Steel by Eddy Current Method: A Statistical Optimization Approach, *Res. Nondestruct. Eval.*, 2018, **29**, p 237–254

Publisher's Note Springer Nature remains neutral with regard to jurisdictional claims in published maps and institutional affiliations.